ACS OMEGA

http://pubs.acs.org/journal/acsodf

Article

Sawtooth Faceting in Rutile Nanowires

Ping Zhou,[#] Yushun Liu,[#] and Guo-zhen Zhu*

Cite This: *ACS Omega* 2022, 7, 10406−10412

Read Online

ACCESS | Metrics & More | Article Recommendations | Supporting Information

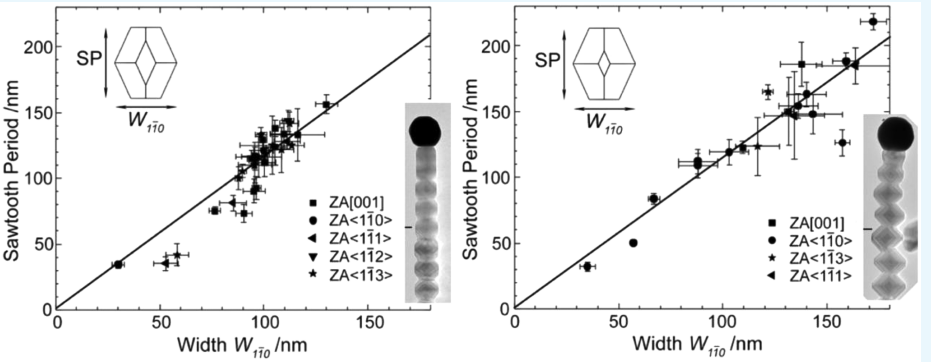

ABSTRACT: Sawtooth faceting, with a diameter-dependent period, is pervasively observed in many Si, III−V, and II−VI nanowires during vapor-phase growth. This can be linked to an oscillation in surface energies, which are influenced by many factors such as crystal anisotropy, surface decoration, and twinning. Without the presence of surface decoration and planar defects, TiO_2 rutile nanowires, axially oriented along a low-symmetry axis of ⟨110⟩, are promising to decouple the effect of crystal anisotropy from other factors. In this work, we synthesized ⟨110⟩ rutile nanowires, which exhibit complex periodic faceting consisting of {101} and {1$\bar{1}$0} facets. In addition to the expected linear width dependence, rutile nanowires, with the same width but different outward-inclined shapes, maintain the same period of their sawtooth faceting, as measured from TEM micrographs. In spite of different surface energy oscillations caused by different shapes, identical nucleation sites, which become energetically favorable during sawtooth growth, are predicted using thermodynamic models for nanowires with different shapes. This finding provides new insights into the morphological control of nanowires.

1. INTRODUCTION

Nanowires, benefiting from their one-dimensional shape at the nanoscale, can functionalize as active components in electronic, optoelectronic, photonic, and magnetic devices as well as chemical sensors.[1] In addition to Si and group III−V nanowires, oxide nanowires have attracted rapidly growing interest because of their superior chemical and mechanical stability.[2,3] The performance of nanowires can be additionally promoted by tuning their crystallographic features, including axial directions and facets, and thus magnifying anisotropic characteristics originating from the crystal lattice of their made materials.[4] Such interplay between crystal anisotropy and wire shape also raises morphology changes, such as crawling, kinking, and sawtooth faceting, during the vapor-phase growth of nanowires.[5−7]

Nanowires generally grow with a cylinder or prism shape, bounded by low-energy facets parallel to the axial direction. In the case of no such suitable facet, nanowires may grow with facets, which are at an angle to the axial direction, and likely, maintain a sawtooth morphology. For instance, Si nanowires, axially oriented along ⟨111⟩, have either parallel facets of {112}[8] or complex sawtooth faceting of {111}/{113}[9−11] or {111}/{100}.[12,13] The appearance of sawtooth faceting can be linked to surface energetics, which is attributed to either changes in the surface chemistry (e.g., decorated by Au clusters,[10,14,15] or B[16]) or periodic oscillations of droplets resulting from the force balance at the trijunction.[17] This sawtooth faceting likely maintains diameter-dependent periodicity. Thermodynamic models predict that the sawtooth period is proportional to the diameter involving the droplet oscillations,[17] while such a period can also decrease with increasing diameter.[12] Both diameter−period relationships are experimentally observed for Si nanowires with Au droplets. The variations in their surface chemistry likely intertwine with the droplet oscillations, together contributing to reported sawtooth faceting.

Received: December 16, 2021
Accepted: March 4, 2022
Published: March 16, 2022

With a reoccurring truncation at the trijunction,[18] kinetic frustration of a droplet can be caused by the N/Ga ratio at the growing GaN nanowire front. Accordingly, ⟨0001⟩-oriented GaN nanowires can exhibit sawtooth morphology consisting of $\{10\bar{1}1\}$ facets, the period of which is roughly proportional to the diameter.[19,20] Although no stacking fault is mentioned in these N-deficient GaN nanowires, stacking faults and twinning, normal to the axial direction, are commonly observed in III−V nanowires, including GaN,[21] GaAs,[22,23] GaP,[23,24] InAs,[25] and InP.[26] These III−V nanowires can also maintain similar sawtooth faceting with periodic stacking faults or twin planes. Instead of minimizing total energies in the above thermodynamic models, the nucleation energies, during sawtooth faceting, are applied to explain the effect of twinning.[26] The predicted period has an exponential relationship with the nanowire diameter, as a result of the probability of sequencing nucleation events. With the involvement of planar defects and other geometrical constraints (i.e., truncations at the trijunction), how crystal anisotropy influences the shape selection of nanowires remains largely unclear.

Although a certain morphology of nanowires can significantly advance their applications, for example, sawtooth faceting for thermal[27] and electronic[24] applications, the affected parameters, such as droplet oscillation, surface decoration, and twinning, have not been fully clarified. Most reported Si, III−V, and II−VI nanowires grow along their high-symmetry axes, the effect of crystal anisotropy can be largely underestimated. In this study, we select a simple and clean model system, i.e., TiO_2 rutile nanowire synthesized by vapor−adsorbate−solid growth,[28] during which only heat treatment of Au-deposited rutile single-crystal substrates is involved. We obtain an identical sawtooth period for two types of rutile nanowires, which differs in their sawtooth shape enclosed by $\{101\}$ and $\{1\bar{1}0\}$ facets. This can be explained by the selection of particular nucleation sites at the front of growing nanowires. Our results deepen understanding on the faceting mechanisms and morphological control of nanowires.

2. EXPERIMENTAL METHODS

2.1. Nanowire Growth. Our recently developed synthesis method,[28] i.e., heat treatment of Au-deposited TiO_2 rutile single-crystal substrates, was adopted to fabricate TiO_2 nanowires. The deposition of Au nanoparticles were achieved via either sputtering Au (namely type I nanowires) or evaporating Au nanoparticle suspensions on substrates (namely type II nanowires). The ⟨110⟩-oriented TiO_2 substrates, with polished surfaces, were purchased from MTI Corporation and carefully cleaned with acetone before Au deposition. Au was sputtered using a Hitachi E-1045 and formed particles during the following heat treatment processes. Au nanoparticle suspensions used in the other method were synthesized by the Turkevich method and dropped and then evaporated on substrates. Although the suspension was carefully washed before deposition, it should be noted that particle suspensions might lead to chemical residuals and therefore could cause a difference in the growth atmosphere. As a result, nanowires synthesized by the above two methods had different outward-inclined shapes. The Au-deposited substrates were transferred to a quartz tube, vacuumed, and then sealed with Ar (99.999% purity) filling at a pressure of 200 Torr. The enclosed vessels were heat treated within a tube furnace at 1000 °C for 1 h and then slowly cooled to room temperature.

2.2. Morphology Characterization. The morphology of nanowires was studied using a scanning electron microscope (SEM, FEI Nova NanoSEM 450). After that, nanowires were scraped from substrates onto copper grids for transmission electron microscopy (TEM) characterization. The TEM characterizations were performed with a FEI TALOS F200X at 200 kV.

2.3. In-Situ Experiments. The in situ heating experiment was carried out using a single-tilt heating holder (Nano ex-i/v, thermo scientificTM). Nanowires were heated to 1000 °C to mimic the growth temperature. After heating, the specimen was cooled to room temperature within seconds.

2.4. Qualitative Measurement. For each nanowire, the sawtooth period and the width were determined by averaging measurements from as many sawtooth segments as possible. The errors of period and width were evaluated separately by the root-mean-square method incorporating the standard deviation Δ_A for multiple measurements and the systematic error Δ_B. The systematic error was taken as the actual length of two pixels at the imaging magnification. A confidence interval of 0.95 was adopted for all measurements.

3. RESULTS AND DISCUSSIONS

3.1. Sawtooth Faceting in Rutile Nanowires. The typical sawtooth morphology of rutile nanowires is examined by scanning electron microscopy (SEM) and transmission electron microscopy (TEM). As shown in Figure 1, these

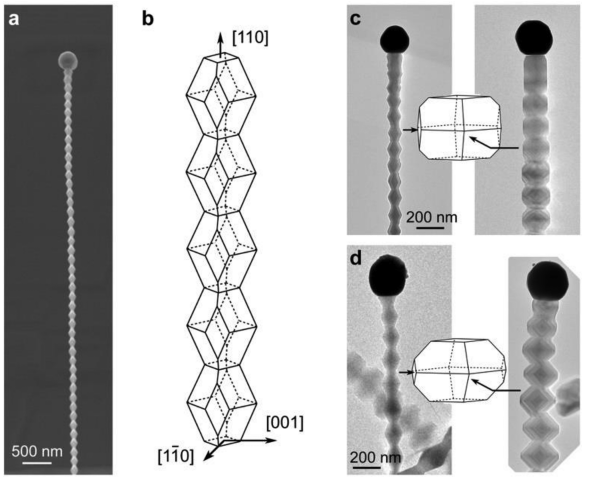

Figure 1. Morphology of rutile nanowire growing along [110]. (a) The SEM image of the rutile nanowire shows the sawtooth sidewall topped with a near spherical Au droplet. The view direction is close to $[1\bar{1}0]$, with a 20° angle of incidence. (b) The crystallographic configuration of rutile nanowire. Each bead is enclosed by eight $\{101\}$ facets and two $\{1\bar{1}0\}$ facets. (c), (d) TEM images of rutile nanowires at zone axes $[1\bar{1}0]$ (left) and [001] (right), respectively, for two different shapes of nanowire classified as type I (c) and type II (d).

nanowires, with the observed width ranging from tens to hundreds of nanometers, maintain alike sawtooth faceting over a few microns in length. At one end of the nanowires, there are near spherical gold seeds, which have slightly larger radii compared to those of the nanowires connected to them. As illustrated in Figure 1b, nanowires are periodically assembled by nearly identical "beads" along $[1\bar{1}0]$, the growth direction. Each "bead" is enclosed by two $\{1\bar{1}0\}$ facets and eight $\{101\}$ facets. It is worth mentioning that the surface energies of rutile

https://doi.org/10.1021/acsomega.1c07119
ACS Omega 2022, 7, 10406−10412

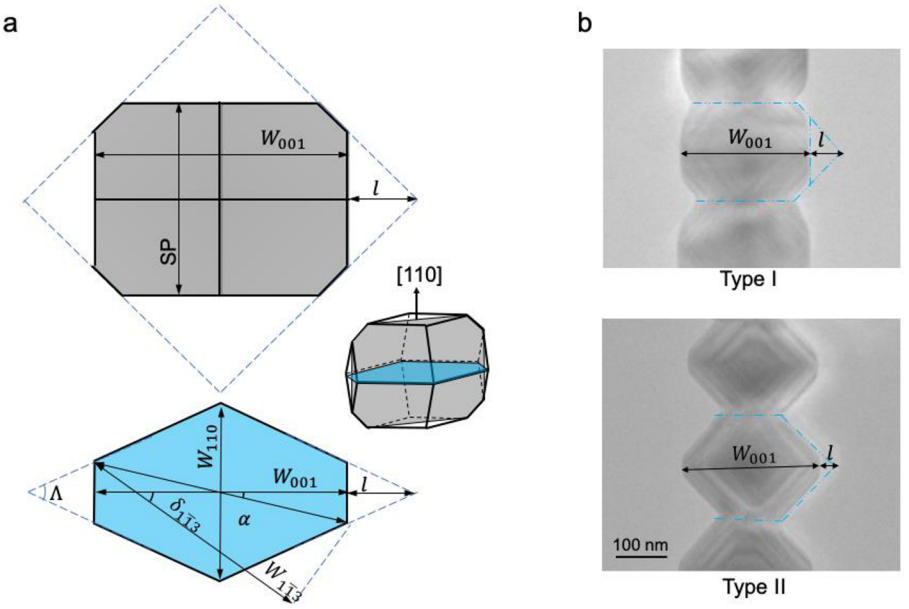

Figure 2. Schematics for the width normalization between different view directions. (a) The bead and its projected area along [001] (the top graph) and along [110] (the bottom graph). These dashed lines denote one set of the intersecting lines of two {101} facets and, therefore, are along ⟨100⟩ (viewed along [001], the top graph) and along ⟨$\bar{1}$11⟩ (viewed along [110], the bottom graph). (b) Experimental measurement for the shape angle α and l in type I and II nanowires viewed at [001].

increase as a sequence of {1$\bar{1}$0}, {100}, and {101} facets, and therefore, the Wulff prediction of rutile crystals can be different from the above "bead" shape.[29] The {1$\bar{1}$0} facets are rhombuses along the growth direction, and the {101} facets are irregular pentagons inclining 22.5° from the growth direction. As a result, the cross-sectional shape of nanowires changes from rhombuses to irregular hexagons to rhombuses periodically. This also causes changes in measured widths obtained from different view directions. It should be noted that all nanowires are single crystals and defect-free. Since {110} is a mirror plane of rutile, no planar defect, such as twinning and stacking fault, can exist between "beads". In addition, no gold adsorbate is detected at any facets of nanowires, even those facets close to the droplet.[28]

Nanowires are different in their outward-inclined shapes caused by slightly differences in growth atmosphere sealed within quartz tubes and consequent differences in surface energies of facets. The main discrepancy lies in the position of {1$\bar{1}$0} facets with respect to the axle center, for nanowires with the same width viewed along [1$\bar{1}$0]. As shown in the schematic drawing in Figure 1c,d, the {1$\bar{1}$0} facets for individual beads can be comparably close to the axle center (classified as type I, Figure 1c) or comparably outward (type II, Figure 1d). Viewed along [001], type I nanowires in the right micrograph of Figure 1c maintain smaller sawtooth undulation than that of type II nanowires in Figure 1d. It is worth noting that the sawtooth morphology of some nanowires is slightly different for a few topmost "beads" near the gold seed, as a possible result of continuous growth during cooling processes. On the other hand, all nanowires have the same morphology viewed along [1$\bar{1}$0], with boundaries defined by the intersecting lines of {101} facets (see the left micrographs in Figure 1c,d). In other words, type I nanowires have maximum widths observed along [001] (i.e., the distance between {1$\bar{1}$0} facets) smaller than those of type II nanowires when the two types have the same morphology and the same width viewed along [1$\bar{1}$0].

3.2. Identical Linear Dependence of Sawtooth Period on Nanowire Width. In order to quantitatively describe the sawtooth morphology of nanowires, the sawtooth period and width are measured for invidual nanowires. The sawtooth period is defined as the length of each "bead" along the axial direction. The width W_{001} is defined as the distance between the two {1$\bar{1}$0} facets of individual "beads", which is also the maximum width viewed along [001]. The width $W_{1\bar{1}0}$ is discribed as the maximum measurement of individual "beads" viewed along [1$\bar{1}$0], together with W_{001} to represent the anostriopic shape of nanowires. Practically, most nanowires can only be observed along a particular view direction, such as [001], [1$\bar{1}$0], [1$\bar{1}$1], [1$\bar{1}$2], or [1$\bar{1}$3] as limited by the tilting angle ranges of TEM holders; therefore, the directly measured widths of nanowires need to be normalized to the width along the same direction (e.g., along [001] and [1$\bar{1}$0]).

To represent the type of nanowires and normalize the measured widths along different directions, we also define a shape angle α as the inverse tangent of the ratio between the short diagonal of {1$\bar{1}$0} facets and W_{001}. According to the crystallographic characteristics of nanowires, $\tan(\alpha) = \frac{2l\cdot\tan\frac{\Lambda}{2}}{W_{001}}$, in which, Λ, with a theoretical value of 49.0°, is the internal acute angle of any {1$\bar{1}$0} facets. l is defined as the distance from the intersecting point of four {101} facets to the {1$\bar{1}$0} facet and can be directly measured from TEM micrographs with acceptable precision (see the labels in Figure 2). The shape angles α are measured as 12.1° and 5.7° for type I and type II nanowires, respectively.

Accordingly, $W_{1\bar{1}0}$ can be linked to W_{001} as follows:

$$W_{1\bar{1}0} = (W_{001} + 2l)\tan\frac{\Lambda}{2} = W_{001}\left(\tan\frac{\Lambda}{2} + \tan\alpha\right) \quad \text{(E1)}$$

https://doi.org/10.1021/acsomega.1c07119
ACS Omega 2022, 7, 10406−10412

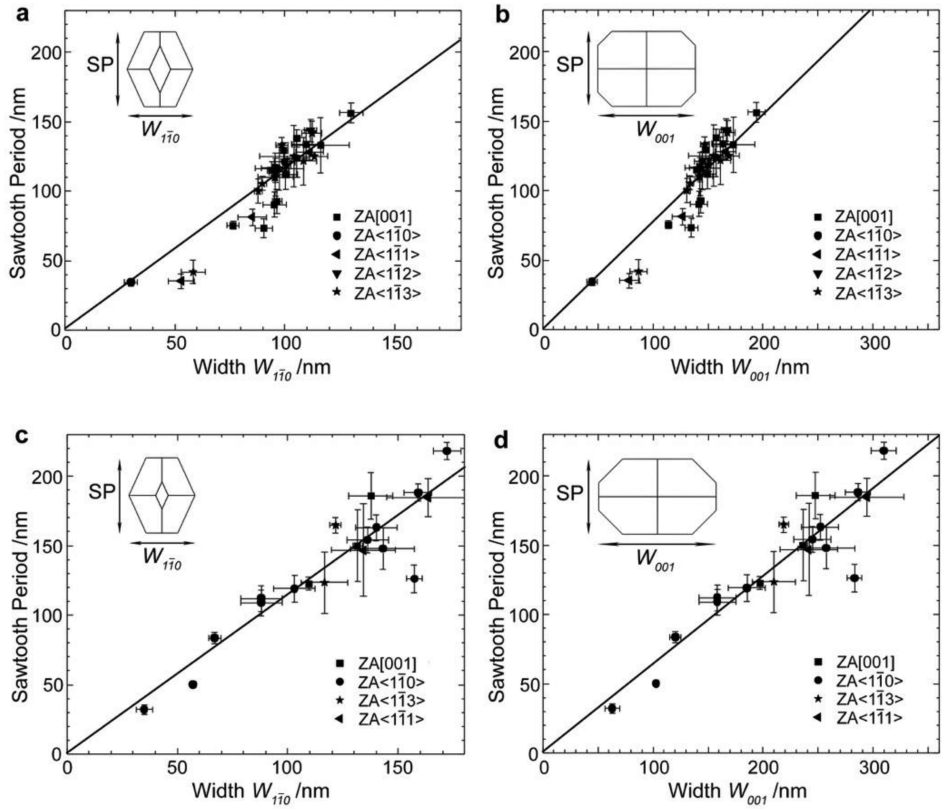

Figure 3. Linear dependence of the sawtooth period on the width for both types. The experimental statistics for type I nanowires are shown as sawtooth period vs width $W_{1\bar{1}0}$ (a) and sawtooth period vs width W_{001} (b). The inserted bead sketches indicate all measurements. The corresponding results for type II nanowires are shown in (c) and (d), respectively.

The maximum widths measured along other view directions, e.g., [1$\bar{1}$1], [1$\bar{1}$2], and [1$\bar{1}$3], are denoted as $W_{1\bar{1}1}$, $W_{1\bar{1}2}$, and $W_{1\bar{1}3}$, which have the following relationships.

$$\frac{W_{1\bar{1}1}}{\cos(\delta_{1\bar{1}1}-\alpha)} = \frac{W_{1\bar{1}2}}{\cos(\delta_{1\bar{1}2}-\alpha)} = \frac{W_{1\bar{1}3}}{\cos(\delta_{1\bar{1}3}-\alpha)} = \frac{W_{001}}{\cos\alpha} \quad \text{(E2)}$$

where, $\delta_{1\bar{1}1}$, $\delta_{1\bar{1}2}$, and $\delta_{1\bar{1}3}$ represent the deviation angles of [1$\bar{1}$1], [1$\bar{1}$2], and [1$\bar{1}$3] with respect to [001]. The values of $\delta_{1\bar{1}1}$, $\delta_{1\bar{1}2}$, and $\delta_{1\bar{1}3}$ are 65.51°, 47.67°, and 36.20°, respectively.

A linear relationship is observed between the sawtooth period and the width of the nanowires, for both type I and type II nanowires, as shown in Figure 3. A total of 31 type I nanowires and 19 type II nanowires are analyzed with widths ranging from tens to hunderds of nanometers. The slopes, K_{001} and $K_{1\bar{1}0}$, are the ratios between the sawtooth period and width W_{001} and $W_{1\bar{1}0}$ through linear fitting of all experimental data. Of particular interest, the slope $K_{1\bar{1}0}$ for type I nanowires is 1.15 ± 0.02, and $K_{1\bar{1}0}$ for type II nanowires is 1.14 ± 0.02, as indicated in the plots in Figure 3a,c and also listed in Table 1. Given the above experimental $K_{1\bar{1}0}$ and shape angle α, $K_{001} = K_{1\bar{1}0}\left(\tan\frac{\Lambda}{2} + \tan\alpha\right)$ can then be computed as 0.77 and 0.63 for type I and type II nanowires, respectively. These values prefectly agree with the measurements in Figure 3b,d, which are 0.77 ± 0.02 and 0.64 ± 0.02 for type I and type II nanowires, respectively. This fact suggests self-consistency in the normalization analysis of the experimental data. In short, type I and II nanowires exhibit the same $K_{1\bar{1}0}$, or in other words, they maintain the same period at a given width (i.e., $W_{1\bar{1}0}$) regardless of their detailed shapes.

Table 1. Geometric Parameters for Sawtooth Faceting of Type I and II Nanowires

NWs	$K_{1\bar{1}0}$	K_{001}	shape angle α (deg)
type I	1.15 ± 0.02	0.77 ± 0.02	12.1
type II	1.14 ± 0.03	0.64 ± 0.02	5.7

3.3. Anisotropic Nucleation at the Growing Nanowire Front. The periodic sawtooth faceting and its linear dependence on width are well explained by thermodynamic models[30] considering either the total energies[9,17] or the nucleation energies.[26] The thermodynamic models involve the contribution from all newly formed facets, the contribution from changes in the horizontal solid−liquid interface under the droplet, and the contribution from changes in droplet surface energy. The first two contributions depend only on the sawtooth facets, which are uniquely linked to the period. The third contribution is determined by the influence of the growth front on the droplet, to a simplified parameter, variations in contact angle β, or the width of this growth front as its primary influencing factor. Thus, a linear period-width relationship is well-defined. (Detailed analysis are in Supplementary B.) It should be noted that the nucleation energies involve additional contributions from changes in the nucleus' perimeter including lateral solid−liquid boundaries. This additional term, together with the first two contributions, depends only on the sawtooth facets, and likely, does not alter the linear relatioship between the period and width. In short, the thermodynamic models are

https://doi.org/10.1021/acsomega.1c07119
ACS Omega 2022, 7, 10406−10412

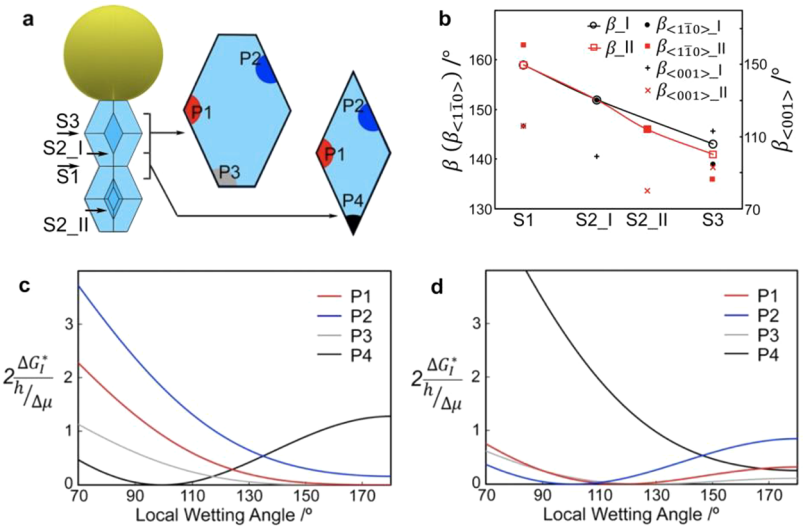

Figure 4. Nucleation at growing rutile nanowire front (a). Potential nucleation sites at different growth fronts. P1−P4 represent the nucleus at acute corners (49°), edges, and obtuse corners (131°) of selected cross sections, respectively. S1−S3 refer to the widening-to-narrowing switch, the appearance of {1$\bar{1}$0} facets, and the narrowing-to-widening switch, respectively. A bead of type II nanowire is overlapped in the bottom bead to show the differences in the two types. (b) Contact angle β and local contact angle β_l as $\beta_{\langle 1\bar{1}0\rangle}$ and $\beta_{\langle 001\rangle}$ at S1−S3 for type I and II nanowires. (c), (d) Estimated nucleation barriers for different sites, with narrowing facets (c) and widening facets (d).

directly applicable to the current rutile nanowires and predict the linear dependence of sawtooth faceting on the width.

On the other hand, type I and II nanowires, prepared by different experimental routes, have different sawtooth shapes. The difference in experimental routes may cause slight differences in growth atmospheres, as a result, surface energies of {1$\bar{1}$0} and {101} facets can be different for type I and II nanowires. It is impossible to measure the differences in surface energies of facets at 1000 °C; however, the surface energies should satisfy $\gamma_{\{1\bar{1}0\}} > \frac{\gamma_{\{101\}}}{\cos\theta}$ to have both {1$\bar{1}$0} and {101} facets. Herein, $\gamma_{\{1\bar{1}0\}}$, and $\gamma_{\{101\}}$ are surface energies of {1$\bar{1}$0} and {101} facets, respectively. θ = 22.5°. The possible differences in surface energies and large variations in the lateral length of {1$\bar{1}$0} and {101} facets likely result in significant differences in total surface energies per lateral length for growing monolayer nanowires. Therefore, the thermodynamic model based on the total surface energies is unlikely to predict the same period−width relationship for type I and II nanowires. (Detailed analysis is in Supplementary B.)

These rutile nanowires grow under extremely low pressure of vapor species, which are generated by thermally vaporizing rutile substrates at high temperature (1000 °C). Thus, the nanowire growth is likely dominated by the formation of a nucleus, instead of their lateral propagation across the growth front. With the contribution from the vanishing existing liquid surface ($\gamma_{LV}\cdot\Delta_{L-I}$, in which γ_{LV} is the liquid−vapor energy and Δ_{L-I} is the vanishing area), heterogeneous nucleation that takes place at the trijunction features a relatively lower energy barrier than the homogeneous nucleation occurring inside. Considering the current rhombus and irregular hexagon growth front, heterogeneous nucleation possibly occurs at their acute corners (P4), obtuse corners (P1, P3), and edges (P2), as illustrated in Figure 4a. With a larger length fraction of the lateral length and subsequently larger Δ_{L-I}, nucleation at acute corners (P4) is energetically preferable without considering sawtooth faceting. As a result, type I and type II nanowires grow differently when {1$\bar{1}$0} facets are involved. However, the influence of sawtooth faceting needs to to be considered during the nucleation process.

Herein, the heterogeneous nucleus is simplified as a circle segment and $\Delta_{L-I} = 2rh$, where r and h are the nonarc edge (i.e., the lateral facets) and height of this circle segment, respectively. As derived in Supplementary C, the nucleation barrier, involving sawtooth faceting, is

$$\Delta G_I^* = \frac{1}{2}\frac{\left[B_I\gamma_{LS} + 2\frac{\gamma_{SV}}{\cos\theta} - 2(\gamma_{LS} + \gamma_{LV}\cos\beta)\tan\theta - 2\gamma_{LV}\right]^2}{2A_I}\frac{h}{\Delta\mu} \quad \text{(E3)}$$

where A_I, B_I, and $\Delta\mu$ are the shape coefficients of area, arc length, and chemical potential for the nucleus, respectively. γ_{SV} refers to the surface energies of involved facets. γ_{LS} refers to the energy of solid−liquid interface. The difference in surface energies between {1$\bar{1}$0} and {101} facets is believed to significantly decrease at high temperatures within the argon atmosphere, as indicated by the reported tendencies.[31,32] Although γ_{SV} can be different for P3, which has one edge on the {101} facet and another on the {1$\bar{1}$0} facet, the same γ_{SV} is applied for simplicity. It should be noted that the involved surface energies are rarely reported at such high temperaures. These values are taken from reports at room temperature, and therefore, no difference in surface energies within the growing atomsphere for type I and II nanowires can be considered. γ_{SV} is approximately 0.5 J/m^2, which is the lowest value among these low-indexed rutile surfaces.[33,34] γ_{LS} = 1 J/m^2 as measured from the shape of Au nanoparticles on flat rutile substrates.[35,36] γ_{LV} = 1.3 J/m^2 referring to droplet surface, which is deduced from the force balance at trijunction. Since γ_{LS} and γ_{LV} are deduced with respect to γ_{SV}, the following tendency is valid although the calculated values cannot be precise due to the uncertainties in γ_{SV}. Accordingly, the nucleation barriers are computed for different nucleation sites, as shown in Figure 4c for narrowing and Figure 4d for widening growth.

The nucleation barrier has clearly a small value at the obtuse corners compared to other nucleation site values, within the involved contact angle ranges (i.e., 140°−160° for β in Figure

https://doi.org/10.1021/acsomega.1c07119
ACS Omega 2022, 7, 10406−10412

4b; experimental measurement and computation details are in Supplementary A) for both narrowing and widening growth. This conclusion holds when one considers the effect of local contact angle by replacing β with the local contact angle β_l. β_l can be different for P1−P4 since spherical droplets are not realistic for the current growth front with anisotropic shapes (i.e., rhombuses or irregular hexagons).[26,37] β_l can be estimated from the droplet simulated by Surface Evolver software.[38] β_l has a value similar to β for obtuse corners (P1, P3) and most edges (P2), while β_l is in the range 80°−110° at acute corners (P4). According to the curves in Figure 4c, nucleation at acute corners may have similar barriers to nucleation at obtuse corners, when $\beta_l \sim 90°$. However, this occurs around the widening-to-narrowing switch, which has an irregular hexagon cross section and no acute corner (P4). Thus, nucleation is favorable at obtuse corners. Figure 4d suggests perferiential nucleations at obtuse corners since the nucleation barrier is much higher at acute corners (P4) when $\beta_l \sim 90°$. In short, the nucleation barrer at obtuse corners is the lowest, resulting in the same nucleation for type I and II nanowires. Once nulceation occurs, its lateral propagation follows quickly across the growth front. As a result, an identical period is predicted for both nanowires, which agrees with the same linear dependence regardless of their detailed sawtooth shapes.

4. CONCLUSIONS

In conclusion, periodic sawtooth faceting and its related width dependence are investigated using rutile nanowires growing along its low-symmetry axis, in order to emphasize the influence of crystallographic anisotropy. The present sawtooth faceting consists of {101} and {1$\bar{1}$0} facets, with changing contributions in surface energies during growth. In addition to the linear wide-period relationship, an identical period is discovered in type I and II nanowires with different outward-inclined shapes. This sawtooth faceting affects the nucleation barriers near the trijunction, resulting in an identical nucleation site for both nanowires. This explains the uniform period of sawtooth faceting regardless of their detailed sawtooth shapes. Our results demonstrate the possibility of controlling nanowire faceting by selecting nucleation sites, opening up avenues of tailoring the morphology of nanowires.

■ ASSOCIATED CONTENT

Supporting Information

The Supporting Information is available free of charge at https://pubs.acs.org/doi/10.1021/acsomega.1c07119.

Droplet simulation, thermodynamic model, and heterogeneous nucleus of a circle segment (PDF)

■ AUTHOR INFORMATION

Corresponding Author

Guo-zhen Zhu − *Department of Mechanical Engineering and Manitoba Institute of Materials, University of Manitoba, Winnipeg, MB R3T 5 V6, Canada;* orcid.org/0000-0002-2910-2786; Email: Guozhen.Zhu@umanitoba.ca

Authors

Ping Zhou − *Department of Mechanical Engineering and Manitoba Institute of Materials, University of Manitoba, Winnipeg, MB R3T 5 V6, Canada; Institute of Materials, China Academy of Engineering Physics, Jiangyou 621908, China*

Yushun Liu − *Department of Mechanical Engineering and Manitoba Institute of Materials, University of Manitoba, Winnipeg, MB R3T 5 V6, Canada*

Complete contact information is available at: https://pubs.acs.org/10.1021/acsomega.1c07119

Author Contributions

P. Zhou, Y. Liu, and G.-z. Zhu conducted experiments and data analysis. G.-z. Zhu supervised the project. All authors contributed to the writing and comments on the manuscript.

Author Contributions

#P. Zhou and Y. Liu contributed to the manuscript equally.

Notes

The authors declare no competing financial interest.

■ ACKNOWLEDGMENTS

We gratefully acknowledge the financial support of University of Manitoba and Canada Research Chair program.

■ REFERENCES

(1) *Nanowires and Nanobelts: Materials, Properties and Devices*; Wang, Z. L., Ed.; Springer US: Boston, MA, 2003.

(2) Shankar, K. S.; Raychaudhuri, A. K. Fabrication of nanowires of multicomponent oxides: Review of recent advances. *Mater. Sci. Eng., C* **2005**, *25*, 738−751.

(3) Nehra, M.; Dilbaghi, N.; Marrazza, G.; Kaushik, A.; Abolhassani, R.; Mishra, Y. K.; Kim, K. H.; Kumar, S. 1D semiconductor nanowires for energy conversion, harvesting and storage applications. *Nano Energy* **2020**, *76*, 104991.

(4) Kuykendall, T.; Pauzauskie, P. J.; Zhang, Y.; Goldberger, J.; Sirbuly, D.; Denlinger, J.; Yang, P. Crystallographic Alignment of High-Density Gallium Nitride Nanowire Arrays. *Nat. Mater.* **2004**, *3* (8), 524−528.

(5) Schwarz, K. W.; Tersoff, J. Elementary Processes in Nanowire Growth. *Nano Lett.* **2011**, *11*, 316−320.

(6) Schwarz, K. W.; Tersoff, J. From Droplets to Nanowires: Dynamics of Vapor-Liquid-Solid Growth. *Phys. Rev. Lett.* **2009**, *102* (20), 206101.

(7) Dubrovskii, V. G.; Cirlin, G. E.; Sibirev, N. V.; Jabeen, F.; Harmand, J. C.; Werner, P. New Mode of Vapor−Liquid−Solid Nanowire Growth. *Nano Lett.* **2011**, *11* (3), 1247−1253.

(8) Moutanabbir, O.; Senz, S.; Scholz, R.; Alexe, M.; Kim, Y.; Pippel, E.; Wang, Y.; Wiethoff, C.; Nabbefeld, T.; Meyer Zu Heringdorf, F.; Horn-Von Hoegen, M. Atomically Smooth P-Doped Silicon Nanowires Catalyzed by Aluminum at Low Temperature. *ACS Nano* **2011**, *5* (2), 1313−1320.

(9) Schwarz, K. W.; Tersoff, J.; Kodambaka, S.; Chou, Y. C.; Ross, F. M. Geometrical Frustration in Nanowire Growth. *Phys. Rev. Lett.* **2011**, *107* (26), 265502.

(10) Xu, T.; Nys, J. P.; Addad, A.; Lebedev, O. I.; Urbieta, A.; Salhi, B.; Berthe, M.; Grandidier, B.; Stiévenard, D. Faceted Sidewalls of Silicon Nanowires: Au-Induced Structural Reconstructions and Electronic Properties. Phys. Rev. B - Condens. *Matter Mater. Phys.* **2010**, *81* (11), 115403.

(11) David, T.; Buttard, D.; Schülli, T.; Dallhuin, F.; Gentile, P. Structural Investigation of Silicon Nanowires Using GIXD and GISAXS: Evidence of Complex Saw-Tooth Faceting. *Surf. Sci.* **2008**, *602* (15), 2675−2680.

(12) Li, F.; Nellist, P. D.; Lang, C.; Cockayne, D. J. H. Dependence of Surface Facet Period on the Diameter of Nanowires. *ACS Nano* **2010**, *4* (2), 632−636.

(13) Oehler, F.; Gentile, P.; Baron, T.; Ferret, P.; Den Hertog, M.; Rouviére, J. The Importance of the Radial Growth in the Faceting of Silicon Nanowires. *Nano Lett.* **2010**, *10* (7), 2335−2341.

(14) Hannon, J. B.; Kodambaka, S.; Ross, F. M.; Tromp, R. M. The Influence of the Surface Migration of Gold on the Growth of Silicon Nanowires. *Nature* **2006**, *440* (7080), 69−71.
(15) Den Hertog, M. I.; Rouviere, J. L.; Dhalluin, F.; Desré, P. J.; Gentile, P.; Ferret, P.; Oehler, F.; Baron, T. Control of Gold Surface Diffusion on Si Nanowires. *Nano Lett.* **2008**, *8* (5), 1544−1550.
(16) Li, F.; Nellist, P. D.; Cockayne, D. J. H. Doping-Dependent Nanofaceting on Silicon Nanowire Surfaces. *Appl. Phys. Lett.* **2009**, *94*, 263111.
(17) Ross, F. M.; Tersoff, J.; Reuter, M. C. Sawtooth Faceting in Silicon Nanowires. *Phys. Rev. Lett.* **2005**, *95* (14), 146104.
(18) Wen, C. Y.; Tersoff, J.; Hillerich, K.; Reuter, M. C.; Park, J. H.; Kodambaka, S.; Stach, E. A.; Ross, F. M. Periodically Changing Morphology of the Growth Interface in Si, Ge, and GaP Nanowires. *Phys. Rev. Lett.* **2011**, *107*, No. 025503.
(19) Ma, Z.; McDowell, D.; Panaitescu, E.; Davydov, A. V.; Upmanyu, M.; Menon, L. Vapor-Liquid-Solid Growth of Serrated GaN Nanowires: Shape Selection Driven by Kinetic Frustration. *J. Mater. Chem. C* **2013**, *1* (44), 7294−7302.
(20) Ding, W.; Meng, X. Growth and UV Detector of Serrated GaN Nanowires by Chemical Vapor Deposition. *Rev. Mex. Fis.* **2020**, *66* (4), 490−495.
(21) Wu, S.; Wu, S.; Song, W.; Wang, L.; Yi, X.; Liu, Z.; Wang, J.; Li, J. Crystal Phase Evolution in Kinked GaN Nanowires. *Nanotechnology* **2020**, *31*, 145713.
(22) Burgess, T.; Breuer, S.; Caroff, P.; Wong-Leung, J.; Gao, Q.; Hoe Tan, H.; Jagadish, C. Twinning Superlattice Formation in GaAs Nanowires. *ACS Nano* **2013**, *7* (9), 8105−8114.
(23) Davidson, F. M.; Lee, D. C.; Fanfair, D. D.; Korgel, B. A. Lamellar Twinning in Semiconductor Nanowires. *J. Phys. Chem. C* **2007**, *111* (7), 2929−2935.
(24) Johansson, J.; Karlsson, L. S.; Patrik T. Svensson, C.; Martensson, T.; Wacaser, B. A.; Deppert, K.; Samuelson, L.; Seifert, W. Structural Properties of ⟨111⟩B -Oriented III-V Nanowires. *Nat. Mater.* **2006**, *5* (7), 574−580.
(25) Caroff, P.; Dick, K. A.; Johansson, J.; Messing, M. E.; Deppert, K.; Samuelson, L. Controlled Polytypic and Twin-Plane Superlattices in III-V Nanowires. *Nat. Nanotechnol.* **2009**, *4* (1), 50−55.
(26) Algra, R. E.; Verheijen, M. A.; Borgström, M. T.; Feiner, L.-F.; Immink, G.; van Enckevort, W. J. P.; Vlieg, E.; Bakkers, E. P. A. M. Twinning Superlattices in Indium Phosphide Nanowires. *Nature* **2008**, *456* (7220), 369−372.
(27) Sansoz, F. Surface Faceting Dependence of Thermal Transport in Silicon Nanowires. *Nano Lett.* **2011**, *11* (12), 5378−5382.
(28) Xie, D. Y.; Lin, M.; Zhou, W.; Wang, J.; Zhu, G. Kinetically Favorable Vapor−Adsorbate−Solid Growth of Rutile Nanowires. *Small Methods* **2019**, *3* (7), 1900111.
(29) Liu, G.; Yang, H. G.; Pan, J.; Yang, Y. Q.; Lu, G. Q.; Cheng, H.-M. Titanium Dioxide Crystals with Tailored Facets. *Chem. Rev.* **2014**, *114*, 9559−9612.
(30) Dubrovskii, V. G. *Nucleation Theory and Growth of Nanostructures*; Springer Verlag: Berlin Heidelberg, 2014.
(31) Mclean, M.; Mykura, H. The Temperature Dependence of the Surface Energy Anisotropy of Platinum. *Sur Sci.* **1966**, *5*, 466−481.
(32) Gheribi, A. E.; Chartrand, P. Temperature and Oxygen Adsorption Coupling Effects Upon the Surface Tension of Liquid Metals. *Sci. Rep* **2019**, *9*, 2365.
(33) Perron, H.; Domain, C.; Roques, J.; Drot, R.; Simoni, E.; Catalette, H. Optimisation of accurate rutile TiO2 (110), (100), (101) and (001) surface models from periodic DFT calculation. *Theor. Chem. Acc.* **2007**, *117*, 565−574.
(34) Jiang, F.; Yang, L.; Zhou, D.; He, G.; Zhou, J.; Wang, F.; Chen, Z.-G. First-principles atomistic Wulff constructions for an equilibrium rutile TiO2 shape modeling. *Appl. Surf. Sci.* **2018**, *436*, 989−994.
(35) Cosandey, F. Epitaxy, Interfacial energy and Atomic Structure of Au/TiO2 interfaces. *Philos. Mag.* **2013**, *93* (10−12), 1197−1218.
(36) Lin, M.; Zhou, W.; Gu, X.; Zhu, G.z. Gold-rutile interfaces with irrational crystallographic orientations. *Mater. Charact.* **2021**, *176*, 111116.
(37) Goktas, N. I.; Sokolovskii, A.; Dubrovskii, V. G.; LaPierre, R. R. Formation mechanism of twinning superlattices in doped GaAs nanowires. *Nano Lett.* **2020**, *20* (5), 3344−3351.
(38) Brakke, K. A. The Surface Evolver. *Exp. Math.* **1992**, *1* (2), 141−165.

https://doi.org/10.1021/acsomega.1c07119
ACS Omega 2022, 7, 10406−10412